Open access • Journal Article • DOI:10.1039/C8FD00146D

Photocatalytic ammonia production enhanced by a plasmonic near-field and hot electrons originating from aluminium nanostructures. — Source link

Madasamy Thangamuthu, Christian Santschi, Olivier J. F. Martin

Institutions: École Polytechnique Fédérale de Lausanne

Published on: 29 May 2019 - Faraday Discussions (The Royal Society of Chemistry)

Topics: Ammonia production and Quantum efficiency

Faraday Discussions

Cite this: *Faraday Discuss.*, 2019, **214**, 399

Photocatalytic ammonia production enhanced by a plasmonic near-field and hot electrons originating from aluminium nanostructures†

Madasamy Thangamuthu, * Christian Santschi and Olivier J. F. Martin

Received 4th October 2018, Accepted 20th November 2018
DOI: 10.1039/c8fd00146d

Ammonia production at room temperature and atmospheric pressure is in high demand to assist in energy saving and the protection of the environment worldwide, as well as to help reduce CO_2 emissions. Recently, plasmonic nanomaterials have been frequently used for solar to chemical energy conversion, which has the potential to replace existing energy-intensive industrial processes. In our approach, plasmonic aluminium nanotriangles (AlNTs) were used to investigate the impact of plasmonic effects on photocatalytic ammonia production. Plasmonic near-field coupling to a semiconductor and hot electron generation from AlNTs were studied in detail through the use of electrochemical photocurrent measurements. A narrowband LED beam with a central wavelength at 365 nm was used to illuminate the AlNTs and their hot electron generation efficiency was estimated to be 2×10^{-4}%, resulting in an ammonia production rate of 4×10^{-5} μM h^{-1} mW^{-1} cm^{-2}, which corresponds to a quantum efficiency of 2.5×10^{-5}%. In the case of plasmonic near-field coupling, AlNTs-embedded TiO_2 demonstrates a charge-carrier generation efficiency of 2.7%, which is ~2.3 times higher than that of bare TiO_2. The ammonia production rate of AlNTs–TiO_2 is 0.1 μM h^{-1} mW^{-1} cm^{-2} with a quantum efficiency of ~0.06%, which corresponds to ~2.4 times that of the rate demonstrated by bare TiO_2 (0.04 μM h^{-1} mW^{-1} cm^{-2}, quantum efficiency ~ 0.025%). The obtained results confirm successful ammonia production through nitrogen splitting at room temperature and under atmospheric pressure. Moreover, according to the presented results, the use of plasmonic aluminium structures remarkably improves the ammonia production rate.

1. Introduction

After photosynthesis, nitrogen fixation is the second most important chemical process in the biosphere, as nitrogen is an essential component of the building

Nanophotonics and Metrology Laboratory (NAM), Swiss Federal Institute of Technology Lausanne (EPFL), CH-1015 Lausanne, Switzerland. E-mail: madasamy.thangamuthu@epfl.ch

† Electronic supplementary information (ESI) available. See DOI: 10.1039/c8fd00146d

blocks of life, *viz.* DNA, RNA and proteins. Unfortunately, direct appropriation from its abundance in the atmosphere (78%) is impossible since the robust triple bond between two nitrogen atoms makes molecular nitrogen relatively inert. The rhizobia bacteria of the legume family and which live in nodules on plant roots possess a nitrogenase enzyme which fixes nitrogen naturally and supplies it to plants and animals in the form of ammonium, urea and nitrate.[1] This naturally occurring process is, however, not sufficient to feed the rapidly expanding population of Earth. For decades the agro-food industry has relied on nitrate fertilizers, produced via the Haber–Bosch industrial synthesis of ammonia (NH_3), to boost food production. In principle, NH_3 can be produced in the presence of catalysts at high temperature (400–600 °C) and pressure (150–200 atm), contributing to approximately 2% of the world's annual energy usage.[2] Furthermore, industrial NH_3 production consumes approximately 5% of the world's natural gas resources to produce a hydrogen feedstock, and releases large quantities of carbon dioxide (CO_2) which strongly pollutes the atmosphere, thus leading to serious environmental issues, *viz.* global warming and climate change *etc.*[3] Therefore, there is strong demand for the development of alternative, fossil-fuel-saving methods that can be utilized to produce ammonia under ambient conditions in order to save energy and the environment.

Numerous researchers have attempted to identify an alternative method to the Haber–Bosch process *via* the use of an electrochemical approach.[4] Recently, Licht *et al.* introduced an electrolysis method in which a sodium and potassium hydroxide solution mixture is bubbled in wet air through a mixture of tiny particles of iron oxide (Fe_2O_3).[5] This method consumes two-thirds of the energy consumed by the Haber–Bosch process and, even more appealingly, CO_2 emissions are significantly reduced in comparison. Although electrochemical routes reduce energy input, they are still under development due to numerous technical challenges and material issues. In another approach, inorganic metal complexes were studied to mimic nitrogenase activity for nitrogen adsorption and reduction.[6,7] However, this route is limited because of the complicated synthesis of the materials and their poor stability. Semiconductor photocatalysis for ammonia production[8–10] has also been highly studied for a few decades after the Fujishima and Honda water splitting experiments were reported.[11] To improve the quantum efficiency and reduce charge-carrier recombination, Khan *et al.* and Ranjit *et al.* studied transition-metal-loaded semiconductors.[12–15] Unfortunately, the efficiency was not significantly improved.

Recently, plasmonic nanomaterials (PNs), a new family of catalysts exhibiting fundamentally different behaviour, have been shown to be highly encouraging due to their optical and catalytic properties under visible light illumination at low intensity. The photocatalytic efficiency can be greatly enhanced by combining PNs with a semiconductor, which increases charge-carrier generation in the semiconductor through plasmonic near-field coupling.[16] Moreover, PNs can solely generate charge-carriers (electron–hole pairs) through non-radiative surface plasmon decay.[17] These so-called plasmonic hot electron/hot hole pairs (EHP) have the potential to drive chemical reactions either on the PNs or on the semiconductor surface, where plasmonic hot electrons can be extracted and transferred to the conduction band of the semiconductor. A Schottky barrier at the metal/semiconductor junction prolongates the residence time of the electrons in the conduction band and, therefore, reduces the fast recombination rate of the

short living EHP.[18] So far, such a plasmonic approach has been successfully applied to improve water splitting,[19] hydrogen dissociation,[20,21] the decomposition of organic pollutants such as carbon dioxide,[22] carbon monoxide[23] and dyes,[24] and the synthesis of organic compounds.[25,26] Recently, Oshikiri *et al.* studied, using light in the visible range, hot electron generation from Au nanoparticles combined with a ruthenium co-catalyst for ammonia synthesis, and encountered a poor yield.[27] In a follow-up study they used zirconium/zirconium oxide, an efficient nitrogen adsorbing material that improved ammonia production significantly.[28] However, Au and Ag are not seminal materials since they are very expensive and unstable over long periods of time, therefore making them inappropriate for long-term use and, consequently, commercialization. Furthermore, the thermal stabilities of Au and Ag are inferior to the stability of Al, therefore rendering Au and Ag unsuitable for high temperature annealing.

In our work we used aluminium as a plasmonic material. Aluminium is a cheap material that exhibits plasmonic properties in the UV range, and is, in comparison with other plasmonic metals, more abundant on earth, highly stable and non-toxic. To the best of our knowledge, we are the first group to study the use of aluminium nanotriangles (AlNTs) for enhancing ammonia production through nitrogen splitting at room temperature and under atmospheric pressure. In order to gain more insight into the plasmonic mechanisms, two different types of photoelectrodes were fabricated to study: (i) plasmonic hot electron generation from AlNTs and (ii) plasmonic near-field coupling to semiconductor materials, such as TiO_2. The charge-carrier generation rate of the photoelectrodes under 365 nm illumination was studied *via* electrochemical photocurrent measurements. An incident photon to photocurrent generation efficiency (IPCE) of 2×10^{-4}% was observed for the hot electron generation by non-radiative decay of surface plasmons, resulting in an ammonia production rate of 4×10^{-5} μM h^{-1} mW^{-1} cm^{-2}, which corresponds to a quantum efficiency of 2.5×10^{-5}%. However, after applying plasmonic near-field coupling, the IPCE increases to 2.7%, which is ~2.3 times higher than that observed when using a bare TiO_2 configuration. The measured ammonia production rate of AlNTs–TiO_2 amounted to 0.1 μM h^{-1} mW^{-1} cm^{-2} with a quantum efficiency of ~0.06%, which is ~2.4 times higher than that obtained with bare TiO_2 (0.04 μM h^{-1}, quantum efficiency ~ 0.025%).

2. Experimental

2.1. Preparation of the photoelectrodes

Plasmonic aluminium nanotriangles (AlNTs) with a side length of 85 nm were fabricated on fused silica substrates *via* colloidal lithography (see ESI† for the detailed fabrication procedure). Due to the high reactivity of Al with oxygen, a self-limiting oxide layer formed on the Al/air interface. Al was deposited *via* electron beam (e-beam) evaporation with a base pressure between 10^{-6} and 10^{-7} Torr (Leybold Optics LAB600H). The thickness and deposition rate of the Al were 40 nm and 0.5 Å s^{-1}, respectively.[29] Subsequently, the PS mask was removed by sonication in toluene for 10 min, followed by the deposition of a 100 nm thick titanium dioxide (TiO_2) thin film onto the AlNTs *via* the e-beam evaporation technique with a deposition rate of 1 Å s^{-1} prior to an annealing step at 500 °C for

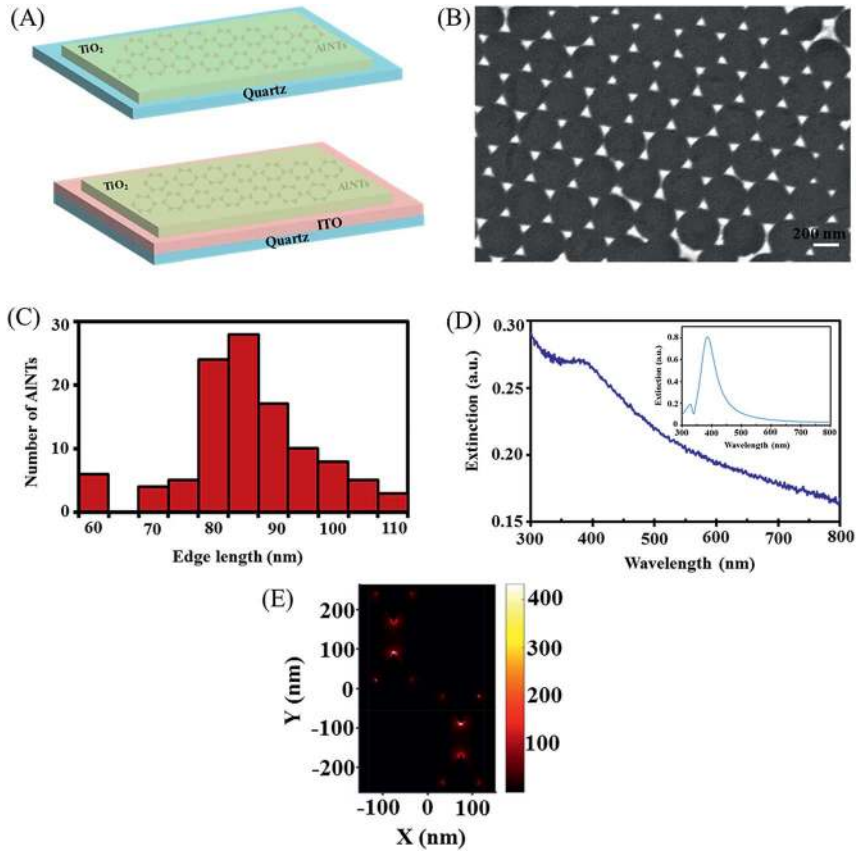

Fig. 1 Characterization of the photoelectrodes. (A) Schematics of the photoelectrodes. (B) SEM image of the AlNTs. (C) Particle size distribution of the AlNTs. (D) UV-Vis-NIR extinction spectrum and the simulated optical spectrum of the AlNTs (inset). (E) Simulated spatial distributions of the electric field enhancement for the AlNTs.

2 h under a nitrogen atmosphere. Fig. 1A shows schematics of the photoelectrodes.

2.2. Characterization

A UV-Vis-NIR spectrometer (UV-2600) with an integrating sphere was used for the extinction, absorption and scattering measurements. The electrical field distribution around the excited AlNTs was computed using the surface integral equation (SIE) method.[30] The real dimension, obtained from the scanning electron microscope (SEM) images, was introduced to calculate the optical responses of the AlNTs. All dielectric coefficients were taken from the literature.[31–33] Morphological SEM images were obtained using a Zeiss Merlin field emission scanning electron microscope (Carl Zeiss Jena GmbH) with an electron energy of 2 keV. X-ray diffraction (XRD) characterization was carried out using an Empyrean diffractometer from Panalytical equipped with a grazing incidence angle configuration and a Cu Kα radiation source ($\lambda = 0.15418$ nm) in order to study the

crystalline structure of the TiO_2. The bandgap energy of the fabricated TiO_2 was calculated using a Tauc-plot. The valence band spectrum of the TiO_2 was obtained using a PHI versaprobe II scanning XPS microscope (Physical Instruments AG, Germany). The analysis was carried out using a monochromatic Al Kα X-ray source of 24.8 W with a beam size of 100 μm, and the binding energy was calibrated using a value for C 1s of 187.85 eV.

2.3. Electrochemical photocurrent study

To perform the electrochemical studies, an electrical conducting layer was added between the substrate and the AlNTs or TiO_2. A 150 nm ITO thin film was deposited *via* radio frequency magnetron sputtering (RF-MS, Pfeiffer SPIDER 600) with an RF power of 500 W and an argon flow of 15 sccm at 5×10^{-3} mbar. The AlNTs embedded in TiO_2 photoelectrodes on ITO were fabricated as described above. Electrochemical measurements were performed using a CHI 1240B potentiostat (CH Instruments, Austin, USA). A three electrode photoelectrochemical cell (Zahner instruments) consisting of a photoanode (working electrode), a Ag/AgCl reference electrode and a platinum counter electrode was used to record the photocurrent. A 0.1 M KNO_3 (pH $\sim$ 6) solution containing 10% ethanol as an electron donor was used as the electrolyte. The working electrode potential was set to 0.15 V *vs.* Ag/AgCl for all of the experiments.

2.4. Photocatalysis experiments

A photochemical cell was used as the reaction chamber. A collimated narrowband LED beam with its central wavelength at 365 nm was used as the irradiation source. The fabricated photoelectrodes were illuminated with an intensity of 5 mW cm^{-2} on a circular area with a diameter of 1.5 cm. Unless otherwise stated, the illumination conditions were the same for all measurements. A nitrogen-saturated aqueous electrolyte solution (pH 4) containing 10% ethanol, an electron donor/hole scavenger, was used for the reaction. The solution contained $\sim$500 μM (saturated concentration) of nitrogen, corresponding to 3×10^{16} nitrogen molecules in the reaction chamber. This concentration was held constant throughout the whole experiment by using a 100 sccm nitrogen flow. The nitrogen gas flow rates were controlled using a mass flow controller (Omega, GmbH). The rate of ammonia production was evaluated by a standard colorimetric assay using sodium salicylate, sodium hypochlorite, sodium nitroprusside and sodium hydroxide. A 500 μL sample was taken from the reaction chamber at 1 h intervals. Subsequently, 250 μL of hypochlorite solution followed by 250 μL of salicylate reagent (a mixture of sodium salicylate, nitroprusside and sodium hydroxide) were added. Sodium salicylate forms a dimer (indosalicylate) in the presence of ammonia, with an absorption peak at 650 nm. Known amounts of ammonium chloride were used to perform a calibration. The value of the ammonia concentration at $t = 0$ h was used as the baseline and subtracted from all measurements. The quantum efficiency of ammonia formation for which three photons are required to produce one ammonia molecule was determined using the following eqn (1)[34]

$$\eta_{NH_3}\ (\%) = \frac{[\text{Rate of } NH_3 \text{ formation } (\text{mol s}^{-1})] \times 3}{[\text{Incident photon flux } (\text{mol s}^{-1})]} \times 100 \quad (1)$$

3. Results and discussion

3.1. Photoelectrodes characterization

An SEM image of the AlNTs is shown in Fig. 1B. Using ImageJ, the size distribution of the AlNTs was statistically evaluated, as shown in Fig. 1C which reveals that the average edge length of the AlNTs is approximately 85 nm, leading to a surface coverage of ~5%. The UV-Vis-NIR extinction spectrum shows a dipolar plasmon peak at around 365 nm (Fig. 1D). The position of the plasmonic resonance wavelength matches well with the simulated spectrum (inset of Fig. 1D).

Furthermore, the SIE near-field simulations show that the highest plasmonic electric field intensities at the resonance position are generated at the edges of the AlNTs (Fig. 1E). The crystalline nature of the TiO_2 was studied before and after annealing using XRD. Fig. 2A displays the XRD pattern for TiO_2 on ITO before annealing. The crystalline peak for anatase TiO_2 is completely absent, indicating that the as-deposited TiO_2 is amorphous. The peaks observed at the 2θ angles of 30.4, 33, 35.34 and 37.65° correspond to the (222), (312), (004) and (114) polycrystalline phases, respectively, of the ITO (JCPDS: 96-101-0342) underneath. However, the XRD pattern of the annealed sample (Fig. 2B) shows an obvious peak at 25.3°, thus confirming the anatase phase (101) (JCPDS: 00-021-1272). A reorganization of the TiO_2 morphology is also evident from analysis of the SEM images (insets of Fig. 2A and B), in which a clear change in the crystal size can be observed. The optical band gaps (E_g) of TiO_2 on the fused silica and ITO substrates were calculated using Tauc plots, as shown in Fig. 2C. The quantity $(\alpha h\nu)^{1/2}$ was plotted as a function of the incident energy and, subsequently, the linear part was extrapolated (see ESI† for details). The resulting point of intersection with the abscissa at 3.18 eV corresponds to the bandgap energy of the deposited TiO_2. The measured bandgap value is in good agreement with the literature.[35] The valence band (VB) spectrum of the TiO_2 was determined *via* XPS analysis (Fig. 2D) in order to obtain the potential at the upper edge of the VB.[35] The VB spectrum shows that the valence band is located at 2.7 eV below the Fermi level, and hence the lower edge of the CB can be expected to be located at 0.48 eV above the Fermi level.

The lower conduction band edge was experimentally determined using photocurrent onset measurements,[36] as shown in Fig. 2E. Under illumination by light at 365 nm (an energy higher than the band gap), TiO_2 generates EHP, which are separated in the potential gradient space-charge layer (formed upon immersing the electrode in the electrolyte). This drives holes towards the TiO_2/electrolyte interface and electrons towards the bulk of the TiO_2 as well as to an external electrical connection (Fig. 2F). Consequently, an anodic photocurrent is observed in the TiO_2 photoelectrode which is affected by an external bias. The potential of the electrode swept in the cathodic direction (applying a more negative potential) reduces the space-charge layer thickness, thus resulting in more charge-carrier recombination and leading to a decreased photocurrent. The photocurrent becomes zero at the flatband potential. In Fig. 2E, the photocurrent reaches zero at −0.1 V with respect to Ag/AgCl, which is equal to −0.335 V *vs.* a standard hydrogen electrode (SHE). For TiO_2, recombination is practically complete 0.2 V away from the CB edge, therefore this value is added to the flatband potential in order to calculate the final CB edge value.[37] Hence, the CB edge of the TiO_2 should be located at −0.54 V above the Fermi level, which is very close

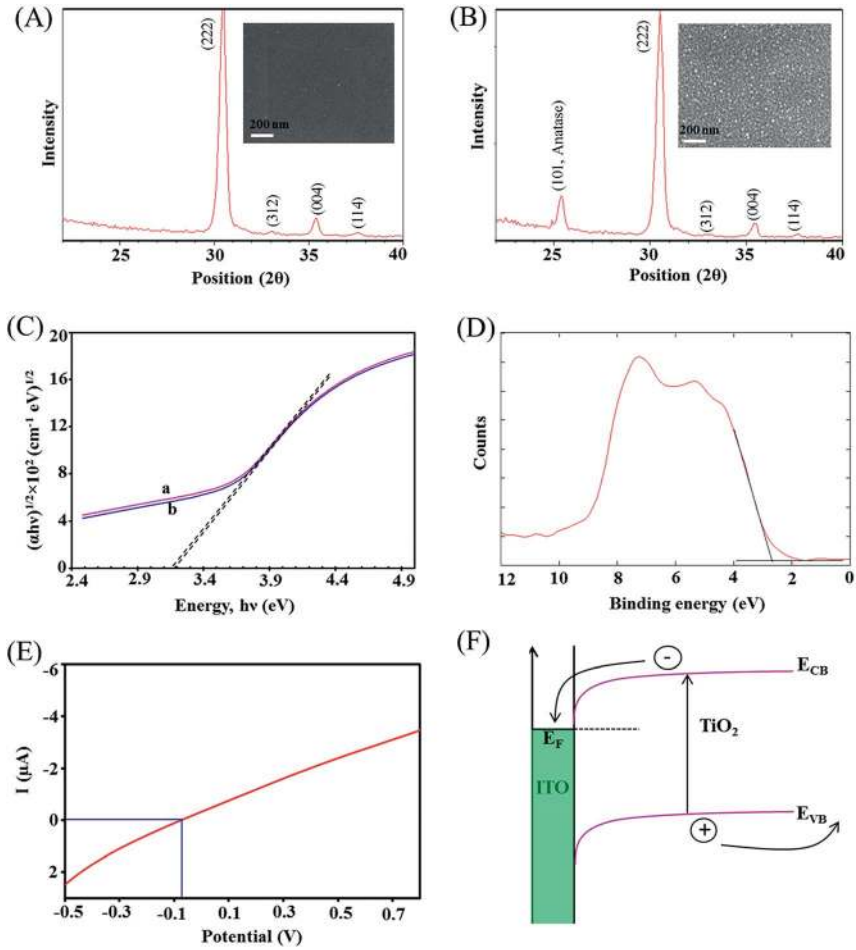

Fig. 2 XRD patterns of the TiO_2 (A) before annealing and (B) after annealing at 500 °C for 2 h under a nitrogen atmosphere (the insets show SEM images of the TiO_2 before and after annealing). (C) Tauc-plot of $(\alpha h\nu)^{1/2}$ as a function of the incident photon energy ($h\nu$) for TiO_2 on the fused silica (a) and ITO (b) substrates. (D) Valence band photoelectron spectrum of TiO_2 (anatase) after annealing. (E) Photovoltammogram of the ITO–TiO_2 electrode recorded in a KNO_3 (0.1 M; pH 6) electrolyte in the cathodic direction with a sweep rate of 2 mV s^{-1} under 365 nm irradiation. (F) Schematic showing the TiO_2 energy levels under illumination.

to the CB edge value deduced from the Tauc-plot. The band diagram of the TiO_2 is depicted in Fig. 3A.

3.2. Electrochemical study of the plasmonic effects of the AlNTs

The plasmonic effects of the AlNTs were studied by means of electrochemical photocurrent measurements. The number of charge-carriers generated in the photoelectrodes is estimated to correspond to a direct measure of their photocatalytic activity.[38] In the first step, we studied plasmonic hot electron generation from the AlNTs. Fig. 3B shows the photocurrent responses of the ITO–AlNTs and

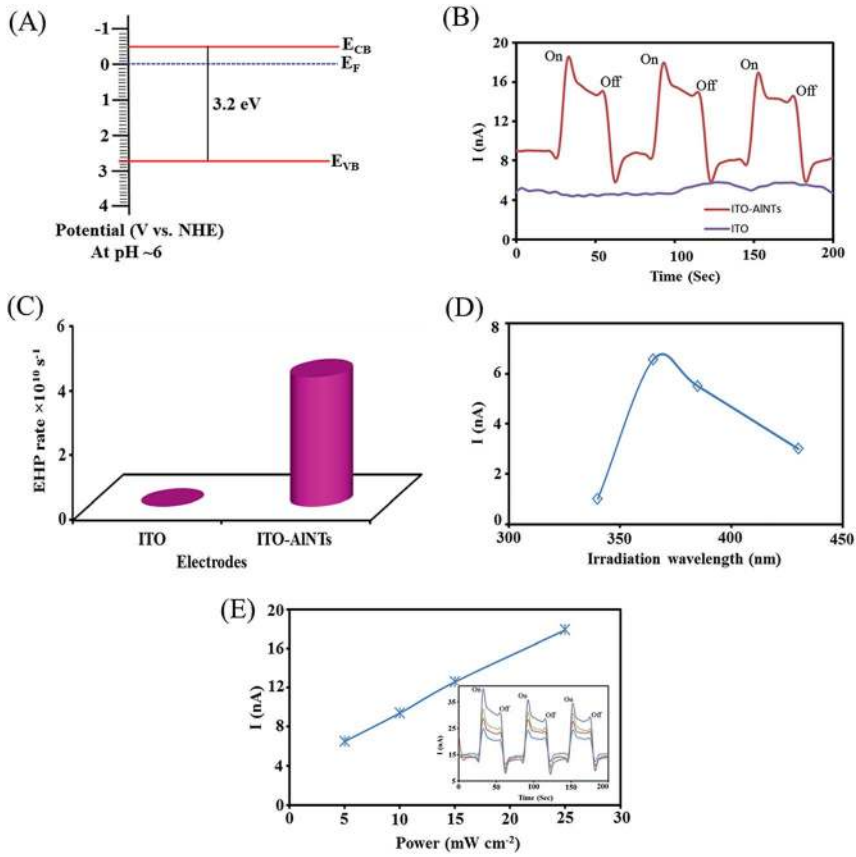

Fig. 3 (A) Energy band diagram of anatase TiO_2 on the electrochemical potential scale; NHE refers to the normal hydrogen electrode. (B) Photocurrent of bare ITO and ITO–AlNTs in a 0.1 M KNO_3 (pH $\sim$ 6) solution containing 10% ethanol, recorded under narrowband irradiation at $\lambda = 365$ nm (5 mW cm^{-2}). (C) Charge-carrier generation rate of the photoelectrodes with and without AlNTs. (D) Wavelength dependent photocurrent of the ITO–AlNTs photoelectrode observed using 340, 365, 385 and 430 nm narrowband light sources at 5 mW cm^{-2} power. (E) Observed photocurrent as a function of light intensity. The inset shows the photocurrent responses of the ITO–AlNTs electrode at 365 nm under different light intensities (from bottom to top: 5, 10, 15 and 25 mW cm^{-2}). The electrodes were biased with 0.15 V for all of the photocurrent measurements.

bare ITO samples. The 365 nm light source was switched on and off every 30 s whilst the photocurrent response was recorded. The obtained currents were stable and reproducible. The ITO–AlNTs sample shows significant photocurrent changes of $\Delta I = 6.5$ nA under illumination, which corresponds to a generation rate of 4×10^{10} hot electrons/holes per second (Fig. 3C) and an incident photon to photocurrent conversion efficiency (IPCE), *i.e.* external quantum efficiency, of 2×10^{-4}%. This result clearly suggests that the AlNTs generate hot electrons as a result of non-radiative surface plasmon decay. The bare ITO does not demonstrate a significant change in current, thus indicating that the illumination wavelength of 365 nm does not excite the ITO. Furthermore the bandgap of ITO is large, around 4 eV, meaning that it certainly requires a higher energy (300 nm

wavelength) to generate charge-carriers; this confirms that the observed 6.5 nA photocurrent is only due to the plasmonic hot electrons from the AlNTs. The wavelength dependent hot electron generation efficiency was also studied using different illumination wavelengths, as shown in Fig. 3D. The maximum current was observed at 365 nm, thus providing further evidence of hot electron generation. To gain more insight into the plasmonic response of the AlNTs, the photocurrent responses at different light intensities were studied. It is clear from looking at Fig. 3E that the AlNTs are linearly responding to the light intensity, which is a characteristic of plasmonic nanomaterials.[39]

In the second step, plasmonic near-field coupling was studied by connecting the AlNTs to TiO_2. Fig. 4A shows the photocurrent responses of the ITO–TiO_2 samples with and without AlNTs under dark and illuminated conditions. For the bare TiO_2 electrode, a photocurrent of $I = 33.2$ μA was observed, corresponding to a generation rate of 2.1×10^{14} EHP per second (Fig. 4B) and an IPCE of 1.1%. The photocurrent response increased to $I = 78$ μA for the sample with AlNTs, corresponding to a generation rate of 4.9×10^{14} EHP per second and an IPCE of 2.7%. Overall, a ~2.3 fold enhancement was observed after embedding the AlNTs into TiO_2, which is also manifested in the increase in the absorption spectrum, as shown in Fig. 4C. The wavelength dependent photocurrent enhancement of the ITO–AlNTs–TiO_2 electrode was determined and is shown in Fig. 4D, which reveals that the enhancement strongly depends on the illumination wavelength, which qualitatively follows the absorption spectrum of the AlNTs (inset of Fig. 4D). The peak position of the photocurrent enhancement and the AlNTs absorption matches very well, thus suggesting that the electromagnetic field located at the edges of the triangles, generated by the dipolar surface plasmon oscillation of the AlNTs, penetrates into the TiO_2, leading to an increased charge-carrier generation rate.

It is worth noting that the AlNTs were in direct contact with TiO_2. The Al and TiO_2 contact exhibits ohmic character since the working function of Al is inferior to that of TiO_2. Therefore, plasmonic hot electron and near-field coupling effects are indistinguishable in the studied configuration. However, the observed results suggest that the hot electron generation and extraction efficiency is very low (2×10^{-4}%) in comparison with the charge-carrier generation efficiency of the near-field coupling (2.7%), thus demonstrating that the contribution from the hot electrons is negligible towards the overall enhancement in the AlNTs–TiO_2 configuration. Furthermore, the contribution from plasmonic scattering was also studied by extracting the scattering and absorption spectra from the total extinction spectrum and carrying out measurements using an integrating sphere. Fig. 4E and F show the absorption and scattering of the AlNTs before and after combining with TiO_2. It can clearly be seen that the scattering cross section is dominant for the AlNTs prior to TiO_2 deposition; however, the absorption becomes dominant after embedding the AlNTs in TiO_2. It seems that plasmonic near-field coupling is the dominating energy transfer channel rather than scattering, which correlates well with a recent report.[40] Furthermore, we studied the thermal contribution during the photocurrent measurements at 365 nm by additionally irradiating the photoelectrodes simultaneously with a $\lambda = 650$ nm narrowband light source where aluminium absorbs light. The observed photocurrent remains stable and looks similar to Fig. 4A, thus revealing the negligible thermal contribution to the enhanced charge-carrier generation rate. The above

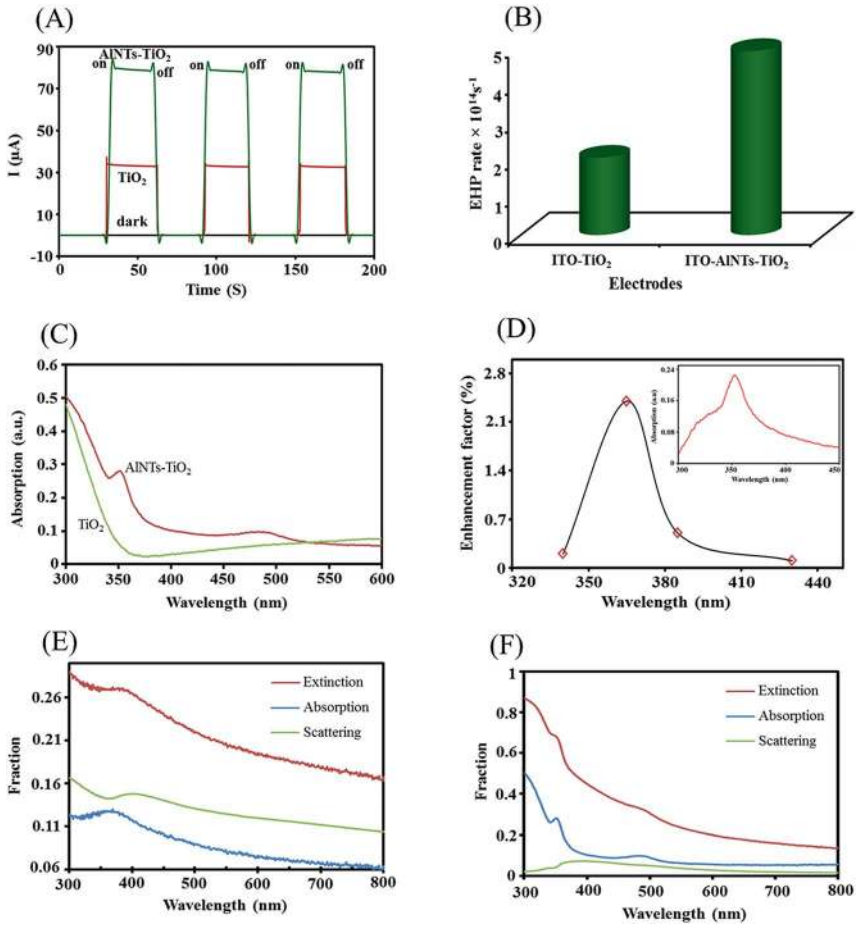

Fig. 4 (A) Photocurrent of ITO–TiO_2 and ITO–AlNTs–TiO_2 in a 0.1 M KNO_3 (pH ~ 6) solution containing 10% ethanol, recorded under narrowband irradiation at $\lambda = 365$ nm (5 mW cm^{-2}) and the dark. (B) Charge-carrier generation rate of the TiO_2 electrodes without and with AlNTs. (C) Absorption spectra of TiO_2 and AlNTs–TiO_2. (D) Wavelength dependent photocurrent enhancement of the ITO–AlNTs–TiO_2 photoelectrode observed when using 340, 365, 385 and 430 nm narrowband light sources; the inset shows the absorption spectrum of the AlNTs extracted from 4C. (E) Absorption and scattering fraction of the AlNTs. (F) Absorption and scattering fraction of AlNTs–TiO_2.

characterizations strongly indicate a predominant contribution of the plasmonic near-field coupling to the enhancement of the charge carrier generation rate.

The stabilities of the fabricated electrodes were evaluated by measuring the photocurrent responses every month over a time period of 6 months. Fig. 5A shows the photocurrent responses of ITO–AlNTs exposed to the conditions used for the hot electron measurements described above. It can clearly be seen that the current response does not change significantly over the first month and decreases subsequently, thus indicating that the hot electron generation efficiency of the AlNTs is reduced with time. It is worth noting that even after 6 months the AlNTs demonstrate 80% of their initial efficiency, thus signifying that Al is more stable

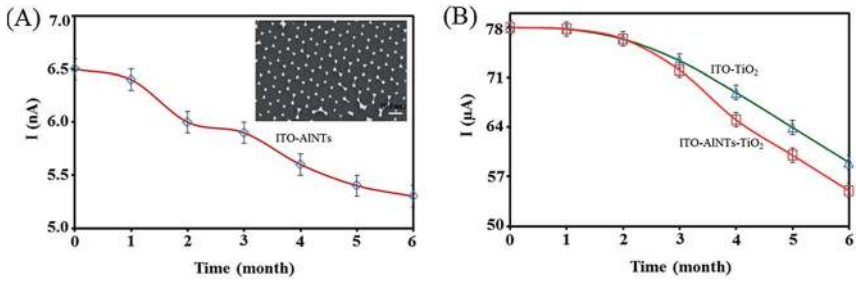

Fig. 5 Photocurrent responses of the (A) ITO–AlNTs and (B) ITO–TiO_2 and ITO–AlNTs–TiO_2 electrodes in a 0.1 M KNO_3 (pH ~ 6) solution containing 10% ethanol, recorded every month under narrowband irradiation at $\lambda = 365$ nm (5 mW cm^{-2}). The inset in Fig. 5A shows an SEM image of the AlNTs recorded 6 months after fabrication.

than Au and Ag. This is due to the fact that the self-limiting oxide (2–3 nm Al_2O_3) protects the structures from further oxidation. Furthermore, Al is insusceptible to surface diffusion, hence the shape of the structures remains, in contrast to Au and Ag,[41] conserved. The inset of Fig. 5A shows an SEM image of the AlNTs taken 6 months after fabrication. Fig. 5B shows a stability study of the ITO–TiO_2 and ITO–AlNTs–TiO_2 electrodes. The photocurrent responses of the TiO_2 and AlNTs–TiO_2 electrodes are reduced to 75% and 70%, respectively, of the initial values.

3.3. Photocatalytic ammonia production

Plasmonic hot electron-driven nitrogen splitting was investigated and the results are shown in Fig. 6A. Under dark conditions, the control experiments revealed no significant ammonia production for the fused silica (FS) without AlNTs. Under illumination, the AlNTs deposited on the fused silica substrates catalyse the production of ammonia at a rate of 4×10^{-5} μM h^{-1} mW^{-1} cm^{-2}, which corresponds to a quantum efficiency of 2.5×10^{-5}%. This clearly indicates that nitrogen splitting takes place at room temperature under atmospheric pressure. The observed ammonia production efficiency is comparable with the hot electron generation efficiency obtained from the electrochemical photocurrent measurements. Fig. 6B shows a schematic of the hot electron-driven charge injection into the nitrogen molecule. Hot electrons are generated from AlNTs as a result of non-radiative surface plasmon decay *via* Landau damping,[42] and are distributed randomly with electron energies at 0 eV to the excitation energy (365 nm) above the Fermi level. Subsequently, hot electrons possessing a suitable energy are transferred into the lowest unoccupied molecular orbital (LUMO) of the adsorbed N_2 molecule and break the N_2 triple bond. The bond breaking mechanism is still not known. The hot electron generation and ammonia production efficiencies are modest, due to the very short lifetime of the hot electrons in the femtosecond range. The hot electrons rapidly lose their energy through electron–electron scattering followed by electron–phonon interactions.[42] Furthermore, the absorption is less dominating in comparison with the scattering for 85 nm edge-length AlNTs, as inferred from Fig. 4E, thus suggesting that surface plasmon decay occurs mainly through a radiative process.

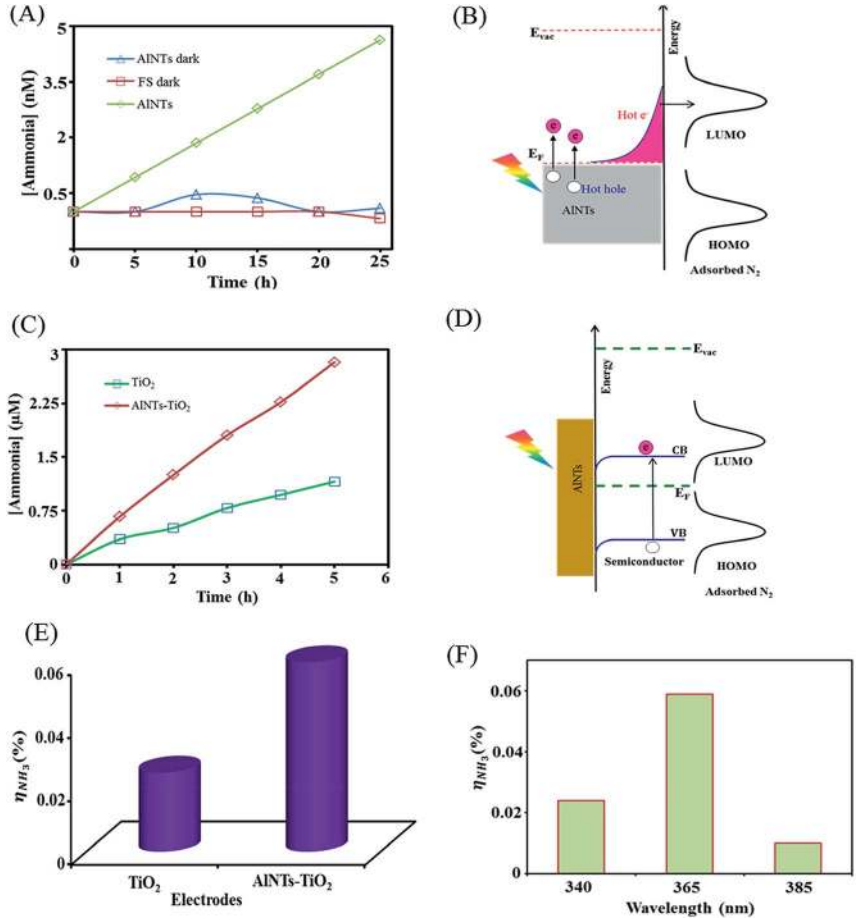

Fig. 6 (A) Plasmonic hot electron-driven ammonia production in a nitrogen-saturated solution (pH $\sim$ 4) containing 10% ethanol under dark conditions and illumination by a narrowband 365 nm beam with a 5 mW cm^{-2} power. (B) Schematic of hot electron-driven charge injection. (C) Plasmonic near-field coupling enhanced ammonia production in a nitrogen saturated solution (pH $\sim$ 4) containing 10% ethanol under illumination by a narrowband 365 nm beam with a 5 mW cm^{-2} power. (D) Schematic of plasmonic near-field coupling enhanced charge injection. (E) Apparent quantum efficiencies of the TiO_2 and AlNTs–TiO_2 photoelectrodes. (F) Wavelength-dependent quantum efficiencies of the AlNTs–TiO_2 photoelectrodes.

In a further step, the effect of near-field coupling on ammonia production was investigated. Fig. 6C shows the ammonia production on the bare TiO_2 and AlNTs–TiO_2 photoelectrodes *versus* time.

Under dark conditions, both electrodes did not exhibit significant differences, whilst under illumination significant ammonia production was observed. It can be seen that ammonia production increases linearly with time, with the production rate estimated to be 0.04 μM h^{-1} mW^{-1} cm^{-2} for bare TiO_2 and 0.1 μM h^{-1} mW^{-1} cm^{-2} for AlNTs–TiO_2. For the AlNTs–TiO_2 sample the reaction rate was observed to be $\sim$2.5 times higher than that for TiO_2, which correlates well with the

photocurrent measurements. Fig. 6D shows a schematic of the plasmonic near-field coupling from the AlNTs to TiO_2. EHP are short-living states leading to a short mean free path, on the order of 50 nm, for the electrons. Hence, the confined plasmonic near-field with its short penetration depth into TiO_2 favours the generation of EHP in the vicinity of the interface and reduces, therefore, the recombination probability. This shallowness has proved to be beneficial for nitrogen splitting. The apparent quantum efficiencies, η, of ammonia production for the TiO_2 and AlNTs–TiO_2 photoelectrodes were calculated, with the results shown in Fig. 6E. The bare TiO_2 and AlNTs–TiO_2 substrates demonstrate, η of 0.025% and 0.06%, respectively. The observed η is significantly higher than what has been previously reported.[34,43–45] Furthermore, the highest η was observed at the plasmonic resonance wavelength (Fig. 6F), revealing again the plasmonic nature of the process. In a control experiment, ammonia production without N_2 replenishment was investigated. Fig. 7A clearly shows the stagnation of ammonia production after the dissolved N_2 is exhausted.

A nitrogen splitting energy diagram is shown in Fig. 7B. The reduction of nitrogen on TiO_2 is thermodynamically possible since the conduction band potential of TiO_2 is at -0.25 V with respect to the SHE at pH 0,[46] which is higher than the potential (-0.092 V) required for N_2 splitting. In our experiments we used pH $\sim$ 4 to ensure the stability of the plasmonic photoelectrode and to provide enough protons for ammonia formation. Under these conditions the conduction band potential is -0.486 V and the nitrogen splitting potential becomes -0.328 V (according to the Nernst equation, *i.e.* $0.059 \times$ pH). Therefore, the energy balance allows for ammonia production under ambient conditions. The possible oxidation and reduction reactions taking place in the potential window are represented by the following equations:

$$h\nu \overset{TiO_2}{\rightarrow} e^- + h^+ \quad (2)$$

$$N_2 + 6H^+ + 6e^- \rightarrow 2NH_3\ (-0.092\ V) \quad (3)$$

$$C_2H_5OH + 2h^+ \rightarrow CH_3CHO + 2H^+\ (0.249\ V) \quad (4)$$

$$2H^+ + 2e^- \rightarrow H_2\ (0\ V) \quad (5)$$

$$4OH^- + 4h^+ \rightarrow 2H_2O + O_2\ (1.23\ V) \quad (6)$$

In addition to nitrogen reduction, the conduction band electrons can reduce protons and evolve molecular hydrogen gas (eqn (5)) since the required potential is well below the conduction band potential of TiO_2. It is well known that TiO_2 is a good photocatalyst not only for nitrogen reduction but also for hydrogen evolution,[47] because both nitrogen and hydrogen adsorb well on the TiO_2 surface. On the other hand, the holes generated in the valence band oxidize hydroxyl radicals leading to the production of water and the evolution of oxygen gas (eqn (6)). To compensate for the electrons used in nitrogen splitting, the electron donor ethanol refills the redundant holes in the VB of TiO_2 (eqn (4)).

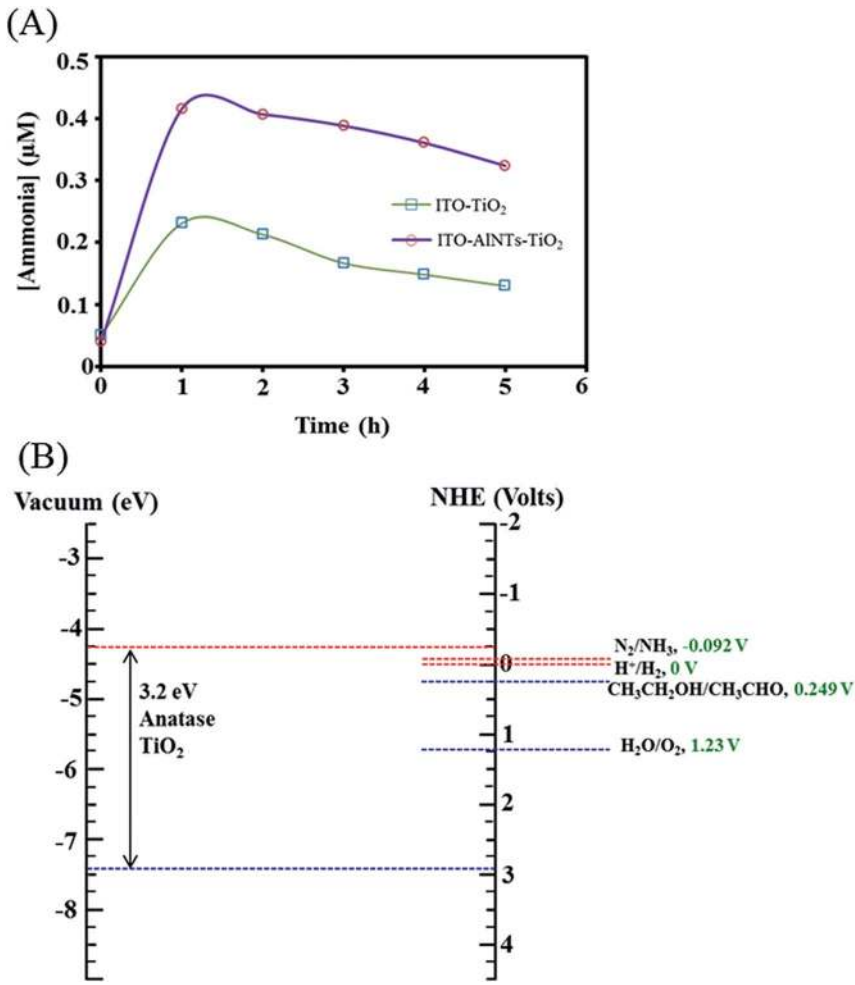

Fig. 7 (A) Ammonia production of irradiated TiO_2 and AlNTs–TiO_2 samples in the absence of a nitrogen gas flow through a nitrogen saturated solution (pH $\sim$ 4) containing 10% ethanol under illumination by a narrowband 365 nm beam with a 5 mW cm^{-2} power. (B) Energy band alignment of anatase TiO_2 and the standard oxidation and reduction potentials of the possible reactions at the band gap energy.

4. Conclusion

We have successfully demonstrated an alternative route for ammonia synthesis through nitrogen splitting at room temperature and under atmospheric pressure using the plasmonic effects of AlNTs. The samples were first characterised *via* SEM, XPS and XRD analysis, thus providing the band energies. The plasmonic hot electron generation from the AlNTs and near-field coupling to a semiconductor were studied in detail by carrying out electrochemical photocurrent measurements. The results revealed that the overall charge-carrier generation efficiency is dominated by a plasmonic near-field coupling effect, when illuminating TiO_2 at a wavelength above the band gap energy. Hot electron-driven ammonia

production was measured to be 4×10^{-5} μM h^{-1} mW^{-1} cm^{-2} with a quantum efficiency of 2.5×10^{-5}%. The AlNTs–TiO_2 photoelectrode exhibits an ammonia production rate of 0.1 μM h^{-1} mW^{-1} cm^{-2}, which is ~2.5 times higher than that of bare TiO_2 (0.04 μM h^{-1} mW^{-1} cm^{-2}), thus indicating enhanced nitrogen splitting at room temperature and under atmospheric pressure. The overall conclusion is that at wavelengths above the band gap energy, the ammonia production rate can be enhanced by a near-field stemming from a plasmonic system, whereas hot electrons play a minor role in such a configuration. The present study offers a large-area AlNTs fabrication method using colloidal lithography, and provides a cheap, efficient and up-scalable method.

Conflicts of interest

There are no conflicts of interest.

Acknowledgements

This project was supported by the Gebert Ruf Stiftung, Switzerland (Grant no. GRS-039/16).

References

1 B. M. Hoffman, D. Lukoyanov, Z.-Y. Yang, D. R. Dean and L. C. Seefeldt, *Chem. Rev.*, 2014, **114**, 4041–4062.
2 S. Ritter, *Chem. Eng. News*, 2008, **86**, 43.
3 A. R. Jawahery, *Energy Efficiency and CO_2 Emissions in Ammonia Production*, International Fertilizer Industry Association, Paris, France, 2009.
4 S. Giddey, S. P. S. Badwal and A. Kulkarni, *Int. J. Hydrogen Energy*, 2013, **38**, 14576–14594.
5 S. Licht, B. Cui, B. Wang, F.-F. Li, J. Lau and S. Liu, *Science*, 2014, **345**, 637–640.
6 J. A. Pool, E. Lobkovsky and P. J. Chirik, *Nature*, 2004, **427**, 527–530.
7 K. Arashiba, Y. Miyake and Y. Nishibayashi, *Nat. Chem.*, 2011, **3**, 120–125.
8 R. I. Bickley and V. Vishwanathan, *Nature*, 1979, **280**, 306–308.
9 O. Rusina, A. Eremenko, G. Frank, H. P. Strunk and H. Kisch, *Angew. Chem., Int. Ed.*, 2001, **40**, 3993–3995.
10 G. N. Schrauzer and T. D. Guth, *J. Am. Chem. Soc.*, 1977, **99**, 7189–7193.
11 A. Fujishima and K. Honda, *Nature*, 1972, **238**, 37–38.
12 K. T. Ranjit, T. K. Varadarajan and B. Viswanathan, *J. Photochem. Photobiol., A*, 1996, **96**, 181–185.
13 M. M. Taqui Khan and N. Nageswara Rao, *J. Photochem. Photobiol., A*, 1991, **56**, 101–111.
14 M. M. Taqui Khan, R. C. Bhardwaj, C. Bhardwaj and N. Nageswara Rao, *J. Photochem. Photobiol., A*, 1992, **68**, 137–146.
15 M. M. Taqui Khan, D. Chatterjee and M. Bala, *J. Photochem. Photobiol., A*, 1992, **67**, 349–352.
16 X.-C. Ma, Y. Dai, L. Yu and B.-B. Huang, *Light: Sci. Appl.*, 2016, **5**, e16017.
17 S. Linic, U. Aslam, C. Boerigter and M. Morabito, *Nat. Mater.*, 2015, **14**, 567–576.

18 M. W. Knight, Y. Wang, A. S. Urban, A. Sobhani, B. Y. Zheng, P. Nordlander and N. J. Halas, *Nano Lett.*, 2013, **13**, 1687–1692.
19 S. C. Warren and E. Thimsen, *Energy Environ. Sci.*, 2012, **5**, 5133–5146.
20 S. Mukherjee, L. Zhou, A. M. Goodman, N. Large, C. Ayala-Orozco, Y. Zhang, P. Nordlander and N. J. Halas, *J. Am. Chem. Soc.*, 2014, **136**, 64–67.
21 S. Mukherjee, F. Libisch, N. Large, O. Neumann, L. V. Brown, J. Cheng, J. B. Lassiter, E. A. Carter, P. Nordlander and N. J. Halas, *Nano Lett.*, 2013, **13**, 240–247.
22 S. Feng, M. Wang, Y. Zhou, P. Li, W. Tu and Z. Zou, *APL Mater.*, 2015, **3**, 104416.
23 K. Li, N. J. Hogan, M. J. Kale, N. J. Halas, P. Nordlander and P. Christopher, *Nano Lett.*, 2017, **17**, 3710–3717.
24 F. Chen, Q. Yang, C. Niu, X. Li, C. Zhang and G. Zeng, *RSC Adv.*, 2015, **5**, 63152–63164.
25 L.-B. Zhao, X.-X. Liu and D.-Y. Wu, *J. Phys. Chem. C*, 2016, **120**, 1570–1579.
26 B. Wu, J. Lee, S. Mubeen, Y.-S. Jun, G. D. Stucky and M. Moskovits, *Adv. Opt. Mater.*, 2016, **4**, 1041–1046.
27 T. Oshikiri, K. Ueno and H. Misawa, *Angew. Chem., Int. Ed.*, 2014, **53**, 9802–9805.
28 T. Oshikiri, K. Ueno and H. Misawa, *Angew. Chem., Int. Ed.*, 2016, **55**, 3942–3946.
29 K. Thyagarajan, C. Santschi, P. Langlet and O. J. F. Martin, *Adv. Opt. Mater.*, 2016, **4**, 871–876.
30 B. Gallinet, A. M. Kern and O. J. F. Martin, *J. Opt. Soc. Am. A*, 2010, **27**, 2261–2271.
31 T. A. F. König, P. A. Ledin, J. Kerszulis, M. A. Mahmoud, M. A. El-Sayed, J. R. Reynolds and V. V. Tsukruk, *ACS Nano*, 2014, **8**, 6182–6192.
32 T. Siefke, S. Kroker, K. Pfeiffer, O. Puffky, K. Dietrich, D. Franta, I. Ohlídal, A. Szeghalmi, E.-B. Kley and A. Tünnermann, *Adv. Opt. Mater.*, 2016, **4**, 1780–1786.
33 A. D. Rakić, *Appl. Opt.*, 1995, **34**, 4755–4767.
34 T. Oshikiri, K. Ueno and H. Misawa, *Angew. Chem., Int. Ed.*, 2014, **53**, 9802–9805.
35 D. O. Scanlon, C. W. Dunnill, J. Buckeridge, S. A. Shevlin, A. J. Logsdail, S. M. Woodley, C. R. A. Catlow, M. J. Powell, R. G. Palgrave, I. P. Parkin, G. W. Watson, T. W. Keal, P. Sherwood, A. Walsh and A. A. Sokol, *Nat. Mater.*, 2013, **12**, 798–801.
36 R. Beranek, *Adv. Phys. Chem.*, 2011, 1–20.
37 J. Schneider, M. Matsuoka, M. Takeuchi, J. Zhang, Y. Horiuchi, M. Anpo and D. W. Bahnemann, *Chem. Rev.*, 2014, **114**, 9919–9986.
38 X. Shi, K. Ueno, N. Takabayashi and H. Misawa, *J. Phys. Chem. C*, 2013, **117**, 2494–2499.
39 P. Christopher, H. Xin, A. Marimuthu and S. Linic, *Nat. Mater.*, 2012, **11**, 1044–1050.
40 U. Aslam, S. Chavez and S. Linic, *Nat. Nanotechnol.*, 2017, **12**, 1000–1005.
41 X. Wang, C. Santschi and O. J. F. Martin, *Small*, 2017, **13**, 1700044.
42 K. Wu, J. Chen, J. R. McBride and T. Lian, *Science*, 2015, **349**, 632–635.
43 M. Ali, F. Zhou, K. Chen, C. Kotzur, C. Xiao, L. Bourgeois, X. Zhang and D. R. MacFarlane, *Nat. Commun.*, 2016, **7**, 1–5.

44 T. Oshikiri, K. Ueno and H. Misawa, *Angew. Chem., Int. Ed.*, 2016, **55**, 3942–3946.
45 H. Zeng, S. Terazono and T. Tanuma, *Catal. Commun.*, 2015, **59**, 40–44.
46 M. Grätzel, *Nature*, 2001, **414**, 338.
47 D. B. Ingram, P. Christopher, J. L. Bauer and S. Linic, *ACS Catal.*, 2011, **1**, 1441–1447.